


RESEARCH

Open Access



Double-activation of mitochondrial permeability transition pore opening via calcium overload and reactive oxygen species for cancer therapy

Ying Zhou^{1,3†}, Shisong Jing^{2†}, Sainan Liu^{3,4}, Xizhong Shen^{5,7}, Lihan Cai^{3,4}, Changfeng Zhu^{5,7*}, Yicheng Zhao^{1,6*}  and Maolin Pang^{3,4*}

Abstract

Background: Calcium ions (Ca^{2+}) participates in various intracellular signal cascades and especially plays a key role in pathways relevant to cancer cells. Mitochondrial metabolism stimulated by calcium overload can trigger the opening of the mitochondrial permeability transition pore (MPTP), which leads to cancer cell death.

Methods: Herein, a mitochondrial pathway for tumour growth inhibition was built via the double-activation of MPTP channel. Fe^{2+} doped covalent organic frameworks (COF) was synthesised and applied as template to grow CaCO_3 shell. Then O_2 was stored into Fe^{2+} doped COF, forming $\text{O}_2\text{-FeCOF@CaCO}_3$ nanocomposite. After modification with folic acid (FA), $\text{O}_2\text{-FeCOF@CaCO}_3\text{@FA}$ (OFCCF) can target breast cancer cells and realize PDT/ Ca^{2+} overload synergistic treatment.

Results: COF can induce the production of $^1\text{O}_2$ under 650 nm irradiation for photodynamic therapy (PDT). Low pH and hypoxia in tumour microenvironment (TME) can activate the nanocomposite to release oxygen and Ca^{2+} . The released O_2 can alleviate hypoxia in TME, thus enhancing the efficiency of COF-mediated PDT. Abundant Ca^{2+} were released and accumulated in cancer cells, resulting in Ca^{2+} overload. Notably, the reactive oxygen species (ROS) and Ca^{2+} overload ensure the sustained opening of MPTP, which leads to the change of mitochondria transmembrane potential, the release of cytochrome c (Cyt c) and the activation of caspases 3 for cancer cell apoptosis.

Conclusion: This multifunctional nanosystem with TME responded abilities provided a novel strategy for innovative clinical cancer therapy.

Keywords: Ca^{2+} overload, MPTP, Hypoxia, Covalent organic frameworks, Photodynamic therapy

*Correspondence: zhuchangfeng@fudan.edu.cn; yichengzhao@live.cn; mlpang@ciac.ac.cn

[†]Ying Zhou and Shisong Jing contributed equally to this work

¹ Center of Infectious diseases and Pathogen Biology, Key Laboratory of Organ Regeneration and Transplantation of the Ministry of Education, The First Hospital of Jilin University, Changchun 130021, China

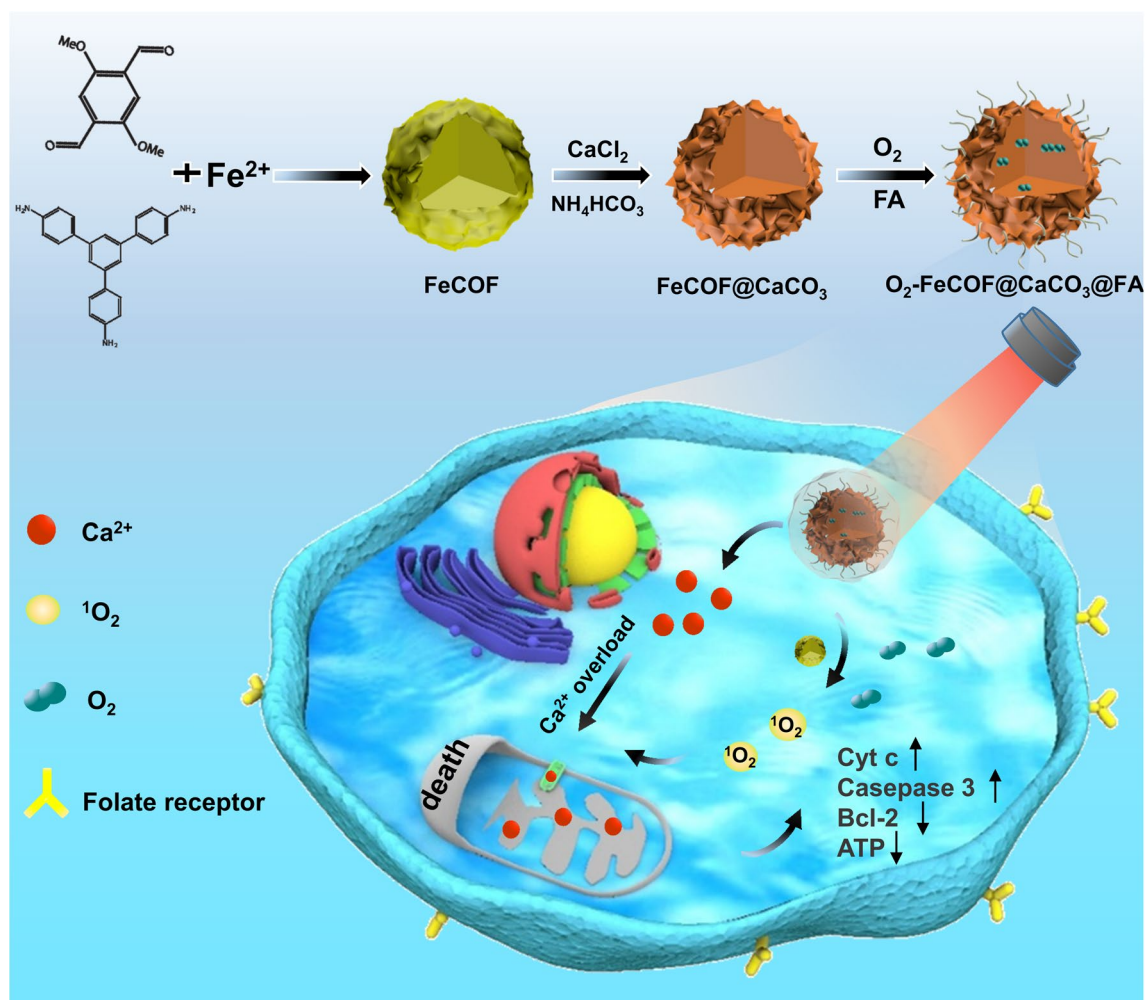
³ State Key Laboratory of Rare Earth Resource Utilization, Changchun Institute of Applied Chemistry, Chinese Academy of Science, Changchun 130022, China

⁵ Department of Gastroenterology and Hepatology, Zhongshan Hospital, Fudan University, Shanghai 200032, China

Full list of author information is available at the end of the article



Graphical Abstract



Introduction

Calcium signal plays an important role in various cancer progression processes such as proliferation, apoptosis and cell migration, which makes the regulation of calcium ions (Ca^{2+}) in cancer cells receive increasing attention [1]. As the second messenger, Ca^{2+} has important effect on cell regulation, which can either induce cell survival or trigger apoptosis [2]. For instance, the fluctuations of Ca^{2+} content in a certain range usually promote cell proliferation and survival, whereas sustained cytosolic calcium induced Ca^{2+} overload can lead to cell apoptosis [3, 4]. Especially, tumor cells are more sensitive to Ca^{2+} overload than normal cells [5–7]. Therefore, it is a promising strategy for triggering intracellular Ca^{2+} overload to realise antitumor therapy.

As one of the intracellular Ca^{2+} pools, mitochondrial uptakes Ca^{2+} depending on the changes of transmembrane potential [8]. Mitochondrial permeability transition pore (MPTP), known as the mitochondrial megachannel, is a non-selective channel across the inner and outer layers of the mitochondrial membrane [9]. It has been reported that the continuous opening of MPTP is the direct cause of cancer cell apoptosis [10]. At physiological levels, Ca^{2+} can activate the transient opening of MPTP, allowing protons or positive ions to enter the mitochondrial matrix to prevent excessive accumulation in the mitochondrial intermembrane space. However, MPTP can be activated to open continuously due to high $[\text{Ca}^{2+}]_m$, high level of reactive oxygen species (ROS) and adenosine triphosphate (ATP) depletion, resulting in mitochondrial and cancer cells dysfunction [11–15].

Obviously, Ca^{2+} is the most important regulator and inductor for MPTP opening [16, 17]. CaCO_3 , a calcium-based biomineralized nanomaterial responding to the tumor acidic microenvironment with pH level as low as 6.2, has excellent degradability and good biocompatibility. As a natural Ca^{2+} reservoir, CaCO_3 can provide sufficient Ca^{2+} source during the process of tumor treatment [18–23]. Moreover, when mitochondrial Ca^{2+} overload occurs, ROS can promote Ca^{2+} to stimulate sustained MPTP opening [24].

Photodynamic therapy (PDT) is a photosensitized reaction with biological effects, which involves oxygen molecules. The process is that the photosensitizer (PSs) absorbed by the tissue is excited by laser irradiation of a specific wavelength, and the excited PSs transfer energy to the surrounding oxygen to produce singlet oxygen ($^1\text{O}_2$) with strong activity. $^1\text{O}_2$ reacts with adjacent biological macromolecules to produce cytotoxicity, resulting in cell damage and even death [25–27]. Compared with conventional treatments such as surgery, chemotherapy and radiotherapy, PDT has the advantages of less trauma, low toxicity and high selectivity [28–30]. However, PDT-mediated continuous oxygen consumption would aggravate hypoxia of cancer cells, which further blunts the therapeutic effect of PDT [31, 32]. Therefore, oxygen storage materials, including hemoglobin [33], perfluorocarbon [34] and metal organic framework (MOF) [35], are used to alleviate hypoxia in tumors.

As an emerging type of porous crystal material, covalent organic frameworks (COF) have been studied for cancer treatment in addition to their conventional applications in energy storage, catalysis, sensing and separation [36]. Owing to their unique structure and characteristics such as porosity, stability and biocompatibility, COF has been widely applied for drug delivery, photodynamic therapy and photothermal therapy [37–40]. Tan and his colleagues, for example, reported a porphyrin-COF for photodynamic therapy of tumors. Under near-infrared irradiation, COF nanoparticles produced abundant ROS to induce cancer cell apoptosis result in their crystalline network structure [41]. Li and his colleagues synthesized a porous 8-hydroxyquinoline functionalized organic covalent framework (COF-HQ) with pH-sensitive tumor microenvironment for 5-FU loading, achieving efficient drug delivery and anti-tumor effects [42]. To the best of our knowledge, the use of COF as a smart carrier for oxygen molecules to achieve tumor-targeted transport has not been reported.

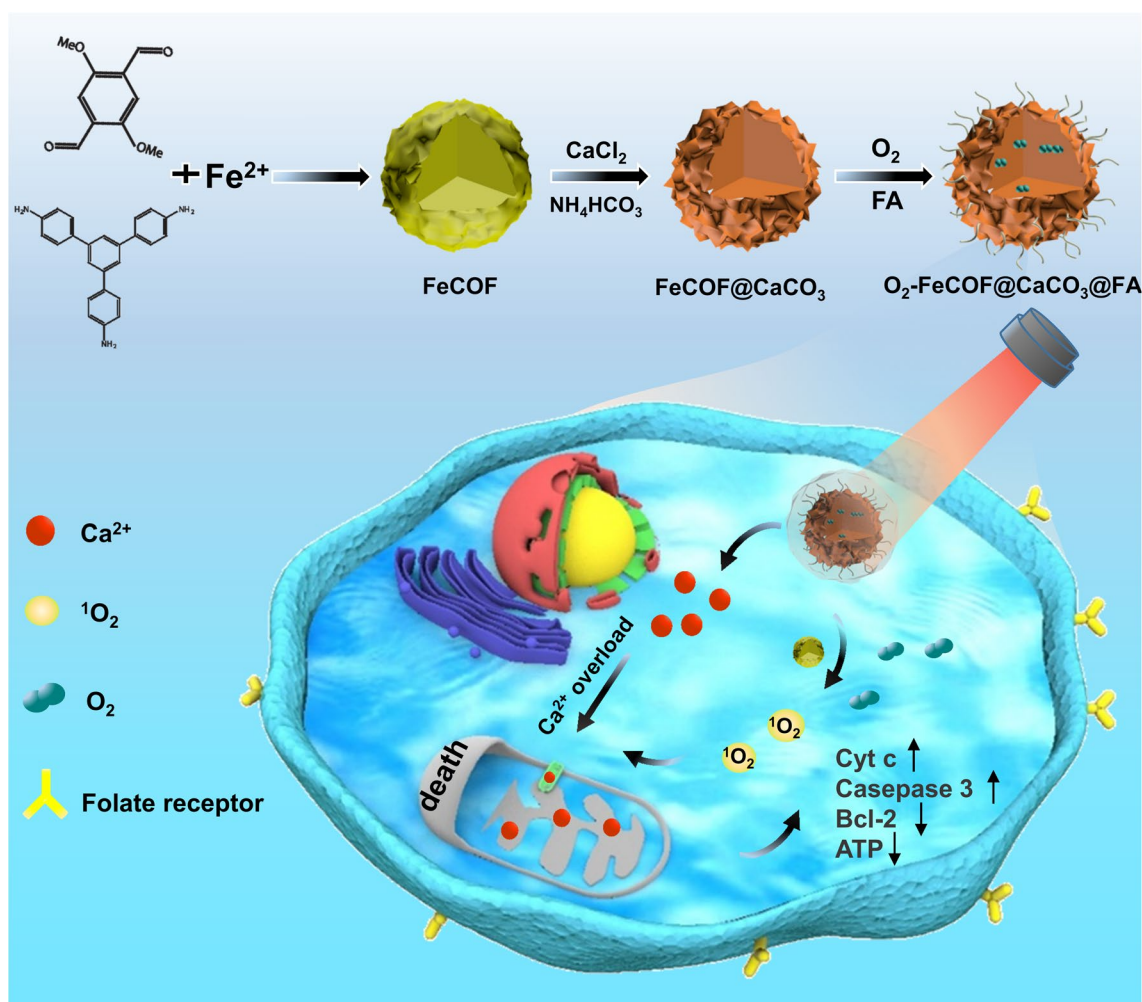
Herein, we synthesized Fe^{2+} -doped COF by Schiff base reaction at room temperature. Then FeCOF was used as a template for the growth of FeCOF@CaCO_3 by gas diffusion method. And folic acid (FA) was modified on the surface of FeCOF@CaCO_3 to form $\text{FeCOF@CaCO}_3@$

FA (FCCF) for achieving targeted therapy against breast cancer. FCCF possessed highly efficient oxygen-carrying capacity owing to the affinity of doped Fe^{2+} with oxygen. Upon internalization into breast cancer cells, $\text{O}_2\text{-FeCOF@CaCO}_3@$ FA (OFCCF) nanoparticles were disassembled, releasing O_2 and Ca^{2+} . COF, as the photosensitizer, was used to produce ROS under light exposure. The released O_2 could enhance COF-mediated PDT in hypoxic tumor microenvironment (TME). Moreover, the coated CaCO_3 layer exhibited excellent pH-dependent dissociation behavior, causing rapid release of Ca^{2+} under the acidic conditions. Large amounts of Ca^{2+} could accumulate in mitochondria, leading to the disruption of Ca^{2+} homeostasis and mitochondria dysfunction. Therefore, the high levels of ROS and intracellular accumulation of Ca^{2+} induced the continuous opening of MPTP, causing an influx of Ca^{2+} to kill cancer cells. Besides, pathological and biochemical tests confirmed that OFCCF nanoparticles could avoid the disturbance of systemic toxicity (Scheme 1).

Results

Synthesis and characterization of $\text{O}_2\text{-FeCOF@CaCO}_3@$ FA NPs

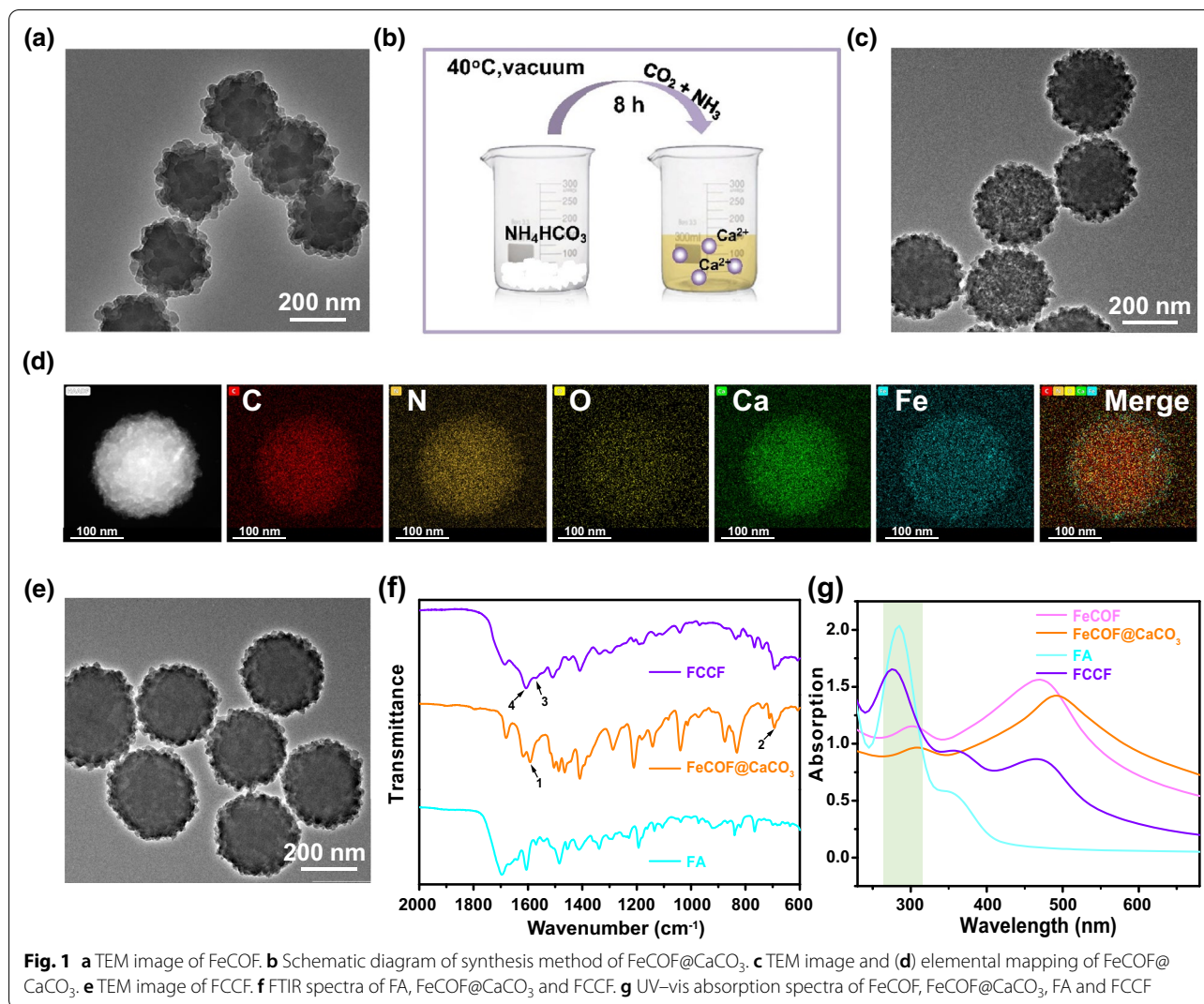
The well-dispersed spherical FeCOF was simply synthesized by using acetic acid as catalyst at room temperature (Fig. 1a and Additional file 1: Figure S1). FeCOF@CaCO_3 was prepared via gas diffusion method. As illustrated in Fig. 1b, in a closed vacuum, the CO_2 and NH_3 gases produced by the natural decomposition of NH_4HCO_3 would continuously diffuse into the mixed solution containing Ca^{2+} . Simultaneously CO_3^{2-} was provided into the alkaline solution to trigger the formation of CaCO_3 [43]. Thin nanosheets of CaCO_3 could be observed on the surface of FeCOF by transmission electron microscopy (TEM, Fig. 1c) and scanning electron microscopy (SEM, Additional file 1: Figure S2). Elemental mapping analysis showed that C, O, N, Fe and Ca elements of FCCF nanoparticles were homogeneously distributed (Fig. 1d). X-ray photoelectron spectroscopy (XPS) was used to analyse Ca element signal of FeCOF@CaCO_3 . The two peaks located at 347.2 eV and 350.7 eV for $2p_{1/2}$ and $2p_{3/2}$, respectively, were considered as the characteristic peaks of CaCO_3 (Fig. S3) [44]. Powder X-ray diffraction (PXRD) patterns have confirmed the excellent crystallinity of FeCOF and FeCOF@CaCO_3 (Additional file 1: Figure S4) [37, 45]. The surface area and pore volume of FeCOF and FeCOF@CaCO_3 were 1380.170 m^2/g , 1.292 cc/g and 373.731 m^2/g , 0.305 cc/g . Compared with FeCOF, FeCOF@CaCO_3 showed decreased Brunauer–Emmett–Teller (BET) surface area and pore volume, confirming the successful coating of CaCO_3 (Additional file 1: Figure S5). Then FA was modified on the surface



Scheme 1 The synthetic route of OFCCF and OFCCF-based Ca^{2+} release and production of $^1\text{O}_2$ activation of MPTP opening inhibits tumor growth strategy

of FeCOF@CaCO_3 to obtain the final FeCOF@CaCO_3 @FA (FCCF) nanoparticles (Fig. 1e). In the FTIR spectra of FeCOF@CaCO_3 , the peak at 1592 cm^{-1} (peak 1) was ascribed to the vibration of $-\text{NH}_2$ and the characteristic peak at 712 cm^{-1} (peak 2) belonged to carbonate. In the FTIR spectra of FCCF, the characteristic peaks at ~ 1573 (peak 3) and 1647 cm^{-1} (peak 4) have been characterized as the stretching vibration mode of secondary amide bonds ($\text{C}=\text{O}-\text{NH}$), further demonstrating the successful synthesis of FCCF (Fig. 1f), further demonstrating the successful synthesis of FCCF [46, 47]. UV-visible (UV-vis) absorption spectrum of FCCF showed that there was a broad absorption between 400 and 700 nm, which was similar to the absorption of FeCOF nanoparticles. Meanwhile, the strong absorbance peak centered at 281 nm of FCCF validated the integration of FA into the

nanosystem (Fig. 1g). TEM and Dynamic light scattering (DLS) measurements showed that the mean size of FCCF was about 230 nm (Additional file 1: Figure S6 and Table S1), slightly larger than that of FeCOF and FeCOF@CaCO_3 nanoparticles. In addition, the successful synthesis of FCCF could also be proved by the zeta potential changes (Additional file 1: Figure S7). The post-modification of FA could enhance the bio-compatible and tumor targeting abilities of FCCF. As shown in Additional file 1: Figure S8, FCCF composite were uniformly dispersed in water, phosphate buffered saline (PBS) and cell culture medium (containing 10% serum) for 7 days without any aggregation at room temperature. The morphology of the nanocomposite had no change even after incubation in water for a week. These results verified the good stability of FCCF for potential clinical applications.

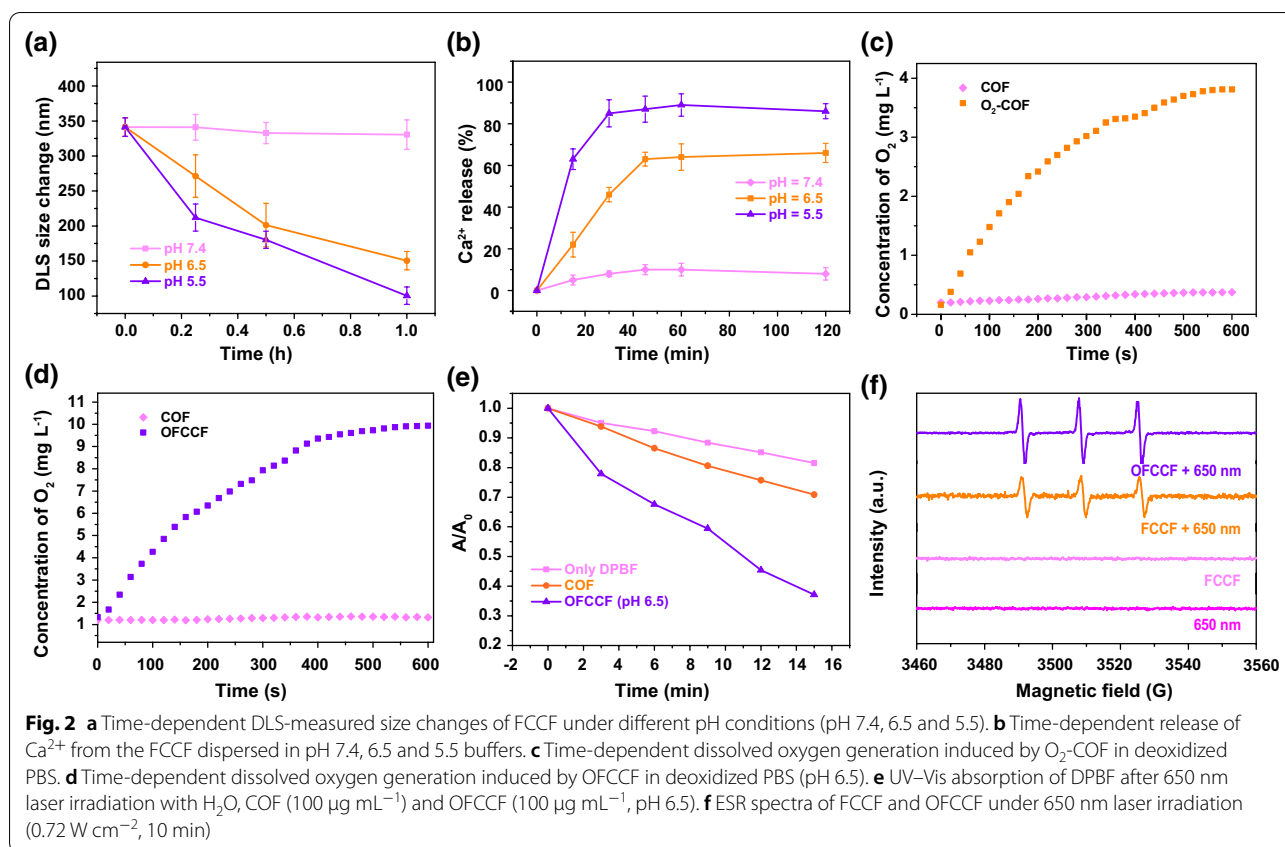


In vitro release study

In order to verify TME-activated bio-decomposition abilities of FCCF nanoparticles, various measurements were conducted. FCCF and FeCOF nanoparticles were dispersed in PBS with different pH to observe the morphology changes at different time points. As shown in Additional file 1: Figure S9 and S10, FCCF nanoparticles showed no change on size and structure when dispersed in PBS at pH 7.4. In contrast, FCCF nanoparticles dissociated in PBS with low pH (6.5 and 5.5), resulting in the nanosheet like morphology of the surface was largely lost after 1 h. Meanwhile, the hydrodynamic sizes of nanoparticles for time-dependent changes were monitored by DLS at different pH values. The hydrated particle of FCCF nanoparticles at pH 6.5 and 5.5 for 1 h were around 180 nm and 100 nm, respectively (Fig. 2a). Then, the time-dependent release profiles of Ca²⁺ were further assessed in buffers with various pH values. As

shown in Fig. 2b, the low pH condition (5.5) led to a sustained release of Ca²⁺, with 89.2% Ca²⁺ being released from FeCOF carrier. However, only about 66.4% Ca²⁺ was released after being incubated at pH 6.5. The above results strongly proved that FCCF exhibited promising pH-responsive Ca²⁺ release ability.

The release of Ca²⁺ further facilitated oxygen diffusion to meet the increased oxygen demand in hypoxic tumor. O₂ releasing ability of OFCCF and O₂-COF in deoxygenated PBS buffer was illustrated in Fig. 2c, d. The stored O₂ of OFCCF and O₂-COF were released under a hypoxic environment by passive transportation. However, the released O₂ from OFCCF was approximately twofold as that from O₂-COF, which was attributed to the affinity of Fe²⁺ with O₂. Moreover, the bubbles produce in the OFCCF solution also demonstrated the specific oxygen release behavior of Additional file 1: Figure S11. The ROS generation ability of OFCCF was investigated by

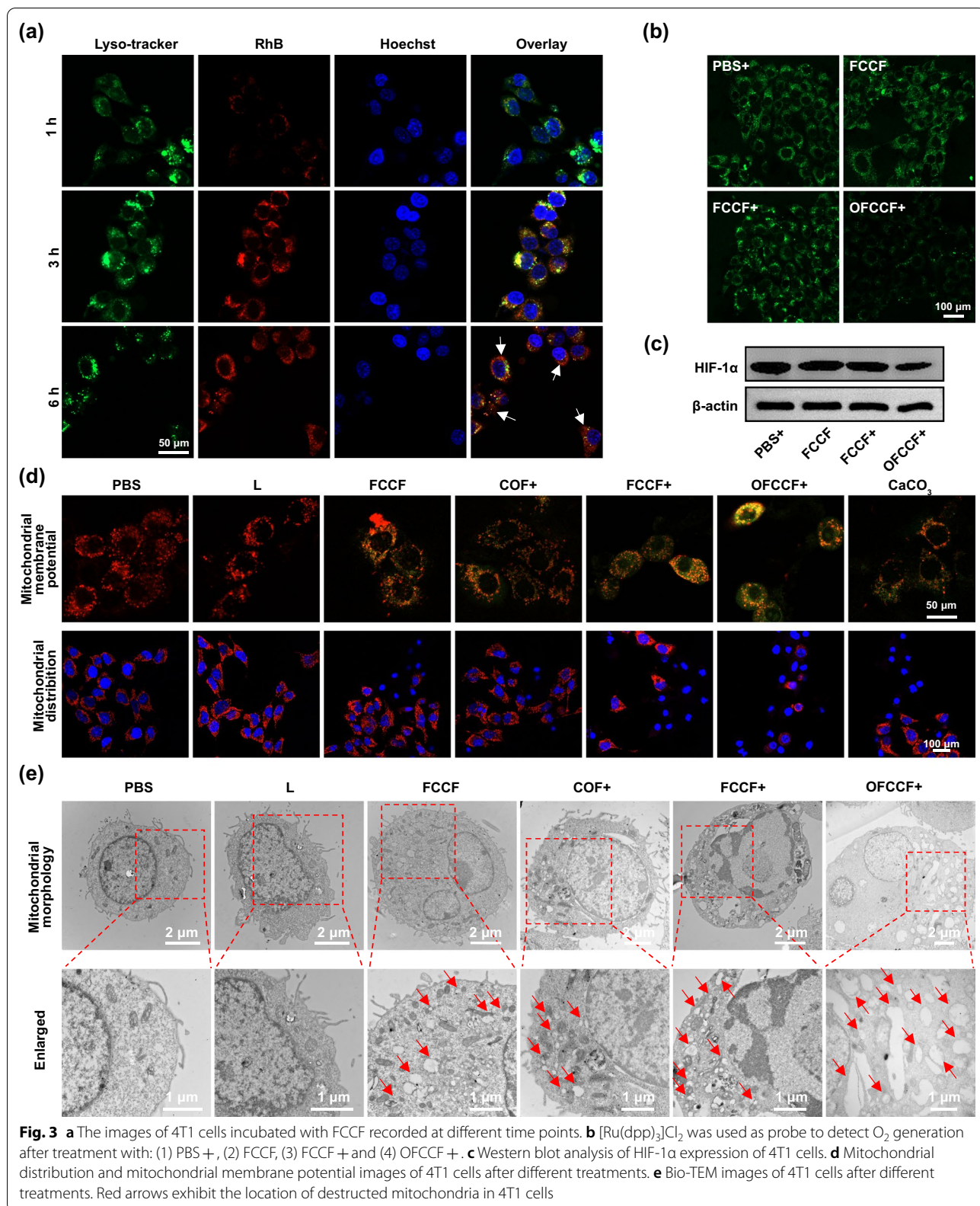


1,3-diphenylisobenzofuran (DPBF). Compared with free DPBF, COF showed effective time-dependent ROS production under 650 nm (0.72 W cm^{-2}) laser irradiation, which was attributed to its strong absorption (Fig. 1g). Moreover, the released O_2 could enhance the production of ROS (Fig. 2e). Next, electron spin resonance (ESR) with 2,2,6,6-tetramethyl-4-piperidinol (TEMP) as singlet $^1\text{O}_2$ trapping agent was used for detecting $^1\text{O}_2$ generation. $^1\text{O}_2$ signal (1:1:1) was observed for OFCCF under 650 nm laser irradiation, which was stronger than that of FCCF (Fig. 2f). Overall, OFCCF with excellent $^1\text{O}_2$ generation ability could effectively overcome tumor hypoxia and enhance PDT effect for breast cancer.

Cancer cell death induced by calcium overload

Next, the cellular internalization of rhodamine B (RhB)-labelled FCCF nanoparticles was examined in murine 4T1 breast cancer cells. Figure 3a indicated the time-dependent internalization process of FCCF nanoparticles, as evidenced by the colocalization of red fluorescence for RhB-labelled FCCF nanoparticles and the green fluorescence for LysoTracker. These results improved that FCCF nanoparticles could be effectively uptaken by 4T1 cells, which was beneficial to killing tumor cells. Within acidic lysosomes, OFCCF nanoparticles could release Ca^{2+}

rapidly, which led to a direct increase of osmotic pressure and influx of Cl^- and H_2O molecules to result in proton sponge effect [21, 46, 47]. Simultaneously, under 650 nm laser irradiation, a large number of $^1\text{O}_2$ were produced by the nanoparticles, causing the destruction of lysosome membrane structure to favor the endosomal escape of nanoparticles. Then, intracellular Ca^{2+} concentration was monitored using the calcium indicator dye Fluo-4. Weak green fluorescence was observed in PBS group and L group of 4T1 cells. In contrast, compared with other groups, the intracellular Ca^{2+} concentration in the OFCCF+ group was highest (Additional file 1: Figure S12). In addition, mitochondrial Ca^{2+} concentrations were quantified using the calcium indicator dye Rhod-2. The FCCF, COF+ and CaCO_3 groups exhibited weak red luminescence, while the group treated with OFCCF+ exhibited strong intracellular luminescence, indicating Ca^{2+} influx of 4T1 cells could be better activated in the presence of ROS (Additional file 1: Figure S13). Via Calcium Colorimetric assay, the OFCCF+ displayed the highest intracellular Ca^{2+} concentration as $19.4 \mu\text{g/mL}$, indicating an obvious Ca^{2+} overloading ($>3.2 \mu\text{g/mL}$ in PBS group) (Additional file 1: Figure S14). The release of Ca^{2+} and the hypoxic tumor microenvironment would trigger the free diffusion of oxygen by



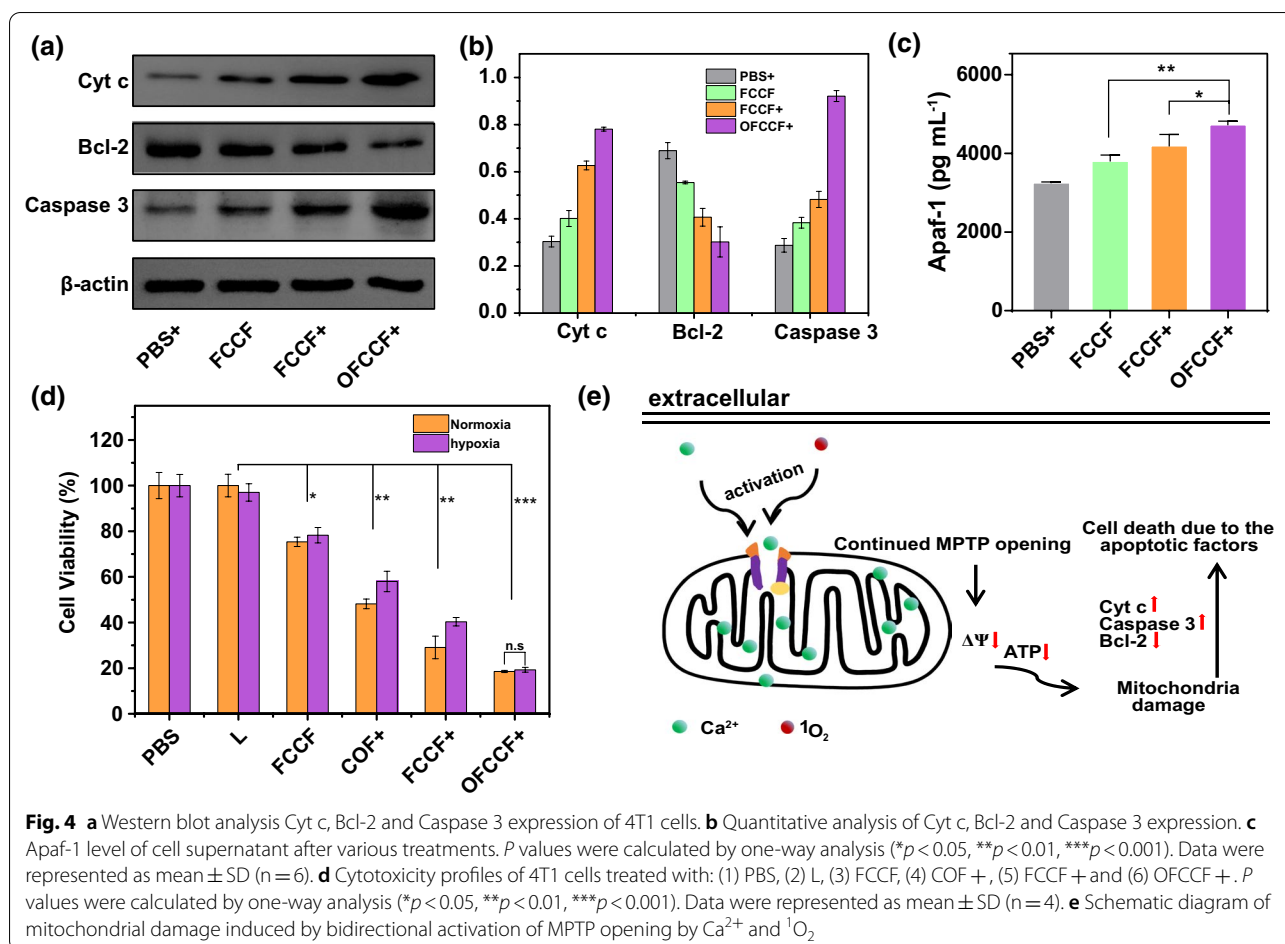
passive-transport. The O_2 probe $[Ru(dpp)_3]Cl_2$ (RDPP) which is prone to luminescence quenching by oxygen was used to monitor cellular O_2 -evolving. As shown in Fig. 3b, the green fluorescence intensity of OFCCF group decreased obviously under hypoxic conditions, while the green fluorescence was observed for L treated and FCCF treated groups. Then, quantitative analysis of dynamic changes of intracellular oxygen via calculating average intensity by ImageJ software. The green fluorescence intensity of 4T1 cells treated with OFCCF+ was 22%, which was about three times lower than the other three groups (Additional file 1: Figure S15). Meanwhile, as the expression of HIF-1 α protein is upregulated under a hypoxic condition, the degree of hypoxia can be further assessed according to the level of HIF-1 α . The OFCCF treated 4T1 cells exhibited a low expression of HIF-1 α by western blotting (WB) analysis (Fig. 3c and Additional file 1: Figure S16). These results suggested that OFCCF could release O_2 to alleviate the hypoxic state of tumor microenvironment. The enhance of ROS generation by OFCCF-mediated O_2 was proved by intracellular 1O_2 test with 2',7'-dichlorodihydrofluorescein diacetate (DCFH-DA) fluorescence as a probe. As shown in Additional file 1: Figure S17, a comparative intensity of green fluorescence was observed under hypoxia and normoxia conditions, suggesting the key role of oxygen release in PDT.

Ca^{2+} overload and 1O_2 can cause the conformational changes of MPTP structural proteins, which allows substances with a molecular weight greater than 1500 to pass through the inner mitochondrial membrane (IMM) by non-selectively way. The entered substances result in the collapse of mitochondrial membrane potential (MMP), the uncoupling of oxidative phosphorylation process and the disturbance of ATP production, consequently causing mitochondria function impairment [16]. Therefore, we used commercial Calcein-AM or Calcein-AM+ $CoCl_2$ dye as a fluorescence indicator to evaluate whether OFCCF was able to induce the continuous activation of MPTP. Upon treatment with FCCF or COF+, green fluorescence was observed. In contrast, no green fluorescence was detected for OFCCF group. However, upon receiving simultaneous exposure of OFCCF+ and 5 μ M uncoupling agent (CCCP), the 4T1 cells exhibited green fluorescence signal (Additional file 1: Figure S18), suggesting the critical role of Ca^{2+} overloading to activate MPTP opening. Next, to reveal the degree of mitochondrial damage induced by enhanced mitochondrial Ca^{2+} overload, the mitochondrial membrane potential of 4T1 cells was evaluated using commercial JC-1 dye. The OFCCF+ group showed strong green fluorescence signal, in marked contrast to the strong red fluorescence observed in other groups. Subsequently, intracellular mitochondrial distribution was detected by staining with Mito Tracker[®] Red

CMXRos. As expected, the fewest mitochondria damage were detected in the OFCCF+ group (Fig. 3d and Additional file 1: Figure S19). Finally, biological transmission electron microscopy (Bio-TEM) was used to visualize changes in their mitochondria (Fig. 3e). The 4T1 cells treated with FCCF, COF+ or FCCF+ exhibited only mild mitochondrial destruction, whereas OFCCF+ caused the most obvious mitochondrial destruction, with visible swelling and cavitation of mitochondria. These results confirm that OFCCF+ can cause severe mitochondrial damage through mitochondrial Ca^{2+} overload. In addition, the intracellular ATP content treated with OFCCF+ decreased significantly in comparison to other five groups, which was partially produced via the oxidative phosphorylation inside the mitochondria (Additional file 1: Figure S20). All of the results revealed that the increased intracellular Ca^{2+} and production of 1O_2 induced by OFCCF+ could cause mitochondrial dysfunction.

The collapse of MMP induces a series of pathological changes in mitochondria, resulting in the release of Cyt c from mitochondrial matrix into cytoplasm. And Cyt c and apoptotic protein activator-1 (Apaf-1) can form a composite to trigger cell apoptosis [48]. To confirm this principle, the expression of apoptosis-related proteins was investigated by western blotting. As illustrated in the Fig. 4a, the expression levels of Cyt c and caspase 3 increased after the treatment of OFCCF+ in comparison to the PBS, FCCF and FCCF+ groups. By contrast, the protein levels of Bcl-2 in 4T1 cells were markedly down-regulated after OFCCF+ treatment. Detailed quantitative results of WB were gathered in Fig. 4b. In addition, the release of Apaf-1 from the supernatant of 4T1 cells was measured by enzyme-linked immunosorbent assay (ELISA). As shown in Fig. 4c, the OFCCF+ treatment elevated the release of Apaf-1 effectively. The above results indicated that mitochondrial-mediated apoptotic pathway was activated after the mitochondrial Ca^{2+} overload and production of 1O_2 .

Then, the cytotoxic effect of COF and FCCF nanoparticles towards L929 fibroblast cells and 4T1 cells was evaluated using the standard methyl thiazolyl tetrazolium assay (MTT). L929 cells were treated with various concentrations of COF and FCCF nanoparticles within 24 and 48 h, the survival rate maintained above 80%. The proliferation ability of L929 cells treated with OFCC+ and OFCCF+ decreased slightly (Additional file 1: Figure S21). These results demonstrated the biosafety and biocompatibility of the nanoparticles. To further investigate the therapeutic effect of Ca^{2+} overload/PDT, the anti-cancer effect of OFCCF under hypoxic and normoxic environment was tested. Upon 650 nm laser irradiation, the cytotoxicity of FCCF+ under

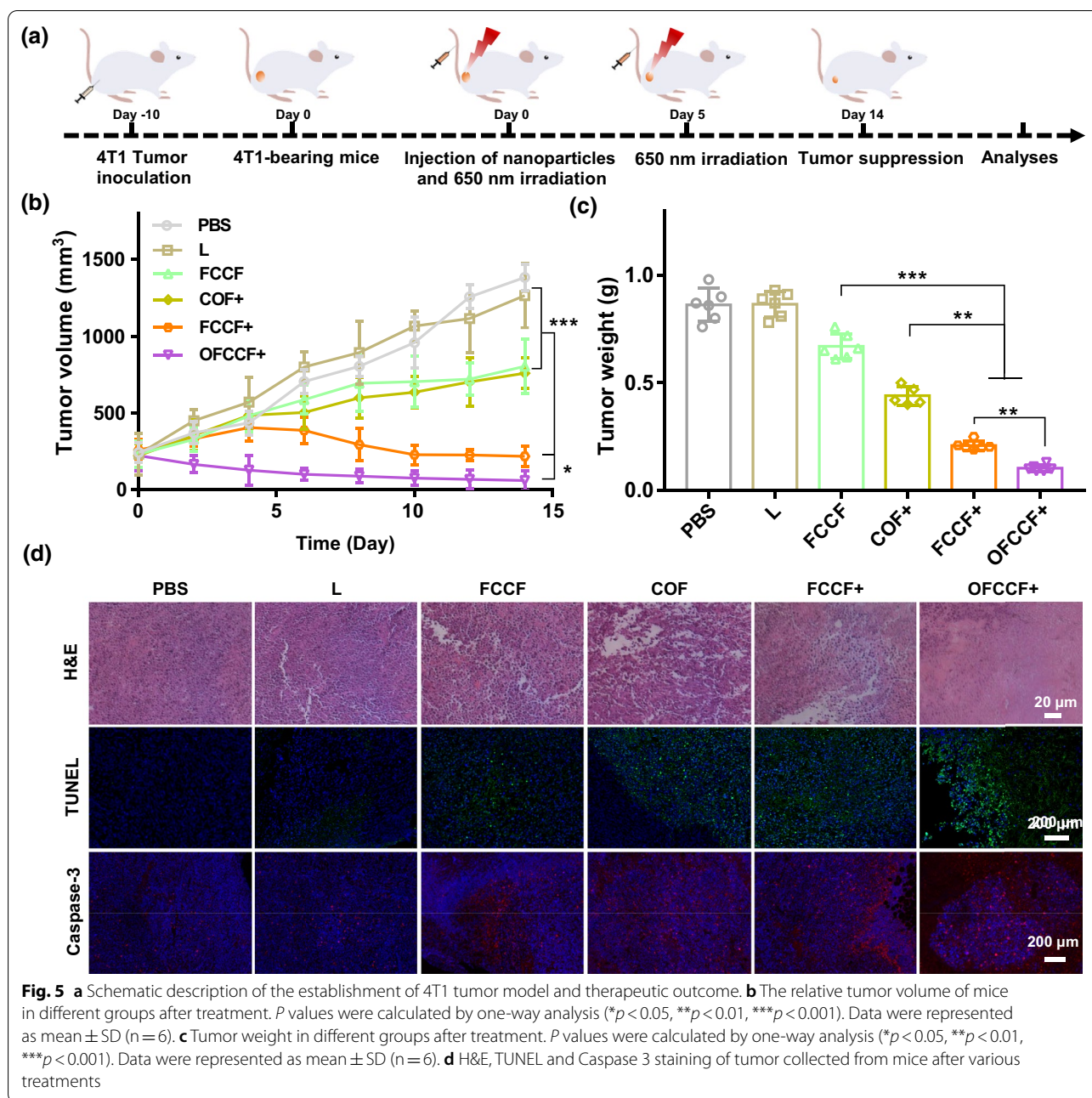


normoxic environment was greatly enhanced than that of FCCF+ under the hypoxic environment. Notably, the hypoxia condition had significant effect on the cancer cell killing effect of FCCF+-treated group. While the survival rate of OFCCF+-treated group was almost the same as the group under hypoxia condition owing to the oxygen-carrying properties of FeCOF (Fig. 4d). Moreover, from the live/dead cell staining test, we observed that most cells remained alive after the treatment of PBS and L. By contrast, the OFCCF+ treated group showed a large number of dead cells in the Additional file 1: Figure S22. This result was consistent with the flow experimental results (Additional file 1: Figure S23). Collectively, all above results reveal that OFCCF is a promising candidate to induce cancer cell death through Ca^{2+} overload and $^1\text{O}_2$ co-activating MPTP opening (Fig. 4e).

In vivo therapeutic effect investigation

The in vivo therapeutic efficacy of OFCCF was further examined by a 4T1 breast tumor model. The tumor-bearing mice were randomly divided into six groups for the different treatments: (1) PBS, (2) 650 nm laser

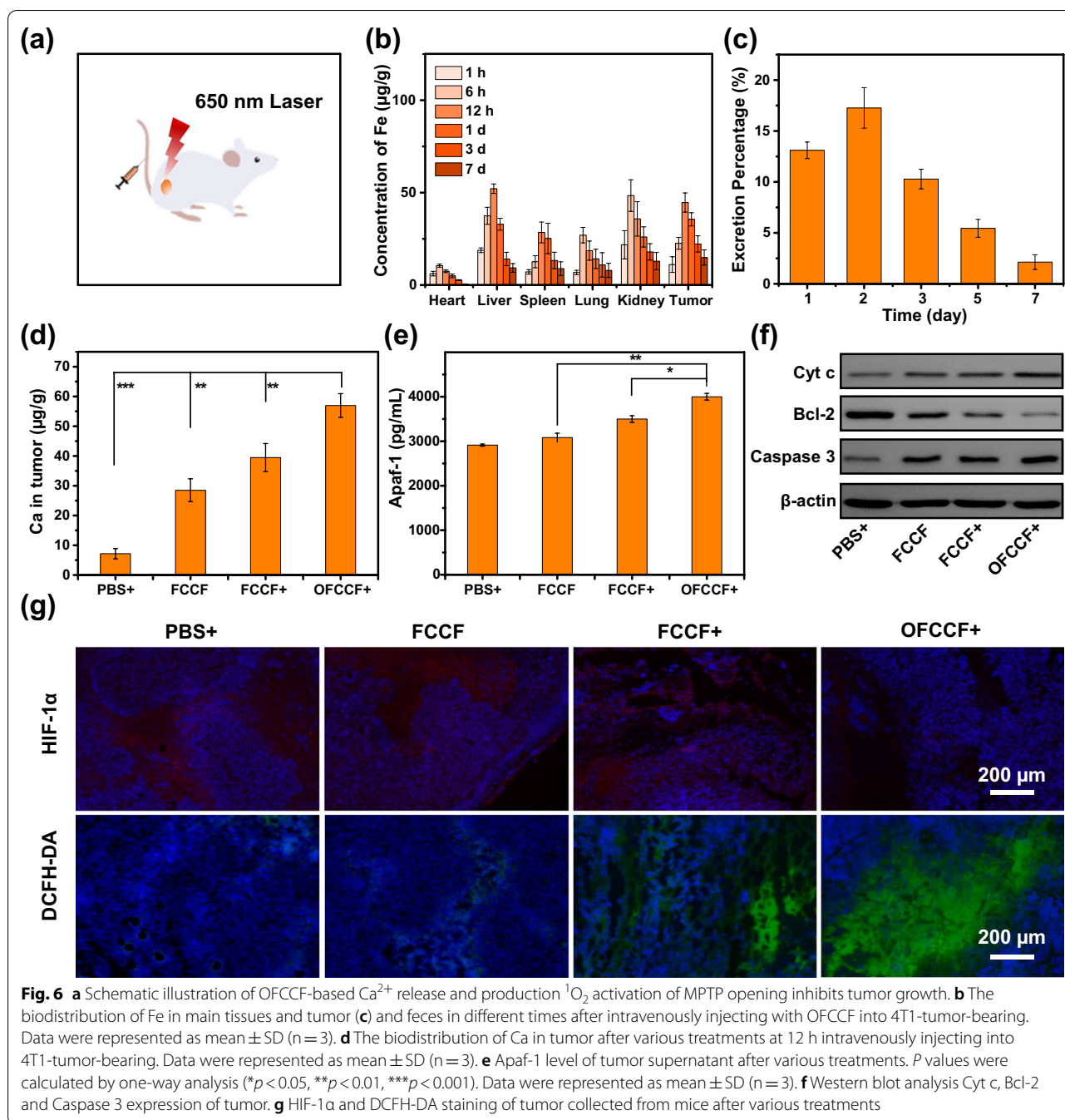
irradiation (L), (3) FCCF, (4) COF+, (5) FCCF+ and (6) OFCCF+. After intravenously injection with nanocomposites ($100 \mu\text{g mL}^{-1}$) for 12 h, the mice were treated with 650 nm laser irradiation (0.72 W cm^{-2}) for 5 min (Fig. 5a). The obtained nanocomposites had no side effect on the body weight of mice, suggesting the good biosafety of the nanocomposites (Additional file 1: Figure S24). Tumor suppression assessments showed a considerable suppression effect on the tumors of FCCF+ group and OFCCF+ group in comparison with other four groups. (Fig. 5b). This result was consistent with the pictures of mice tumors and tumor weight (Fig. 5c and Additional file 1: Figure S25). Furthermore, hematoxylin and eosin (H&E) staining results were shown in Fig. 5d, obvious cell necrosis and apoptosis could be observed in OFCCF+ group. From the TUNEL staining results, the green signal represented that cells apoptosis was appeared after the treatment of OFCCF+. Meanwhile, the typical morphology of apoptotic cells was detected in caspase 3 staining assay. Finally, to better assess the effect of this synergistic therapy, we next examined the lung metastasis of 4T1 tumor-bearing mice after various



treatments. H&E staining and imaging of lung sections confirmed that OFCCF+ effectively suppressed tumor metastasis (Additional file 1: Figure S26).

Moreover, the therapeutic efficiency of OFCCF+ was further evaluated (Fig. 6a). To study the bio-distribution of FCCF, FCCF was injected intravenously into 4T1-tumor-bearing mice and Fe content was tracked by inductively coupled plasma mass spectrometry (ICP-MS). As shown in Fig. 6b, nanoparticles preferentially accumulated at the tumor site due to the specific

binding of FA with breast cancer folate receptors, showing the highest content at 12 h after injection. Apart from tumors, the nanoparticles were also accumulated in liver and kidney. As shown in Fig. 6c, the content of FCCF nanoparticles in liver and kidney decreased gradually, confirming that they could be metabolized from the body through the renal-urinary clearance system within one week. The tumor accumulation and clearance performance of FCCF provides enormous potential for effective and safe cancer treatment. Furthermore, the



bio-degradation performance of nanoparticles triggered by TME was further studied. After the PBS, FCCF and OFCCF was injected intravenously into 4T1-tumor-bearing mice for 12 h, respectively, the Ca^{2+} released from nanoparticles accumulated in tumor owing to the acidic condition of TME. As we expected, the Ca^{2+} content in the tumors significantly increased after being treated with OFCCF+ in comparison to FCCF and FCCF+ groups. It is further revealed that the production of ROS could

promote the aggregation of Ca^{2+} , resulting in the apoptosis caused by Ca^{2+} overload (Fig. 6d). Next, the possible mechanism of Ca^{2+} overload-induced apoptosis was explored by ELISA and western blotting to determine the content of apoptosis-related proteins of tumours. Once Cyt c is released from the mitochondria, it can couple with Apaf-1 to form the apoptosome. As illustrated in Fig. 6e, the upregulation of Apaf-1 confirmed the formation of apoptosome. Besides, the expression levels of Cyt

c, Bcl-2 and caspase 3 were further detected by western blotting. As illustrated in the Fig. 6f, compared with the control groups (PBS, FCCF and FCCF+), Cyt c and caspase 3 expressions levels increased significantly but the protein levels of Bcl-2 decreased after OFCCF+ treatment. The quantitative analysis of western blotting was shown in Additional file 1: Figure S27. Compared with the other groups, the ATP level of OFCCF+ group decreased significantly owing to Ca^{2+} overload in mitochondria, which would damage the energy supply of cancer cells (Additional file 1: Figure S28). To identify the ability of OFCCF to relieve tumor hypoxia, mice tumors were obtained for HIF-1 α (green) staining assay after being injected with the nanoparticles for 10 h. As illustrated in the Fig. 6g, the intensity of fluorescence was hardly visible in OFCCF+ group. For ROS staining assay, OFCCF+ group showed the strongest DCFH-DA fluorescence signals in tumor slices, which was consistent with the HIF-1 α (green) staining assay results. Meanwhile, the remission of tumor hypoxia was further verified by down-regulation of HIF-1 α expression level, indicating that released oxygen could relieve intratumoral hypoxia and enhance production of ROS (Additional file 1: Figure S29).

To assess the potential therapeutic toxicity of FCCF, a systemic toxicity study was performed. The physiological pathology of main organs were analysed by H&E staining. No significant pathological changes in major organs (heart, liver, kidney lung, and spleen) were observed after different treatments (Additional file 1: Figure S30), suggesting the excellent biosafety of the nanocomposite in vivo. Meanwhile, biochemical analysis further confirmed that OFCCF+ had low toxicity (Additional file 1: Figure S31).

Conclusion

In summary, we have successfully prepared an OFCCF nanocomposite with two-way activation of MPTP opening by ROS and Ca^{2+} overload for precise targeted therapy of breast cancer. OFCCF with tumor-targeting ability could effectively aggregate at the tumor sites. The subsequent rapid release of Ca^{2+} and oxygen were attributed to the hypoxia and low pH of TME. Overflowed Ca^{2+} rapidly accumulated inside the cytoplasm, which led to Ca^{2+} influx and activated MPTP opening. Upon NIR light irradiation, the released oxygen could enhance the effect of COF-mediated PDT, and the generation of ROS could promote the activation of MPTP opening. Notably, these two activation mechanisms ensured the sustained opening of MPTP, leading to the change of mitochondria transmembrane potential, release of Cyt c and activation of caspases 3, thus inducing cell apoptosis. Additionally, for the first time, we utilized FeCOF with hypoxia

responsive as oxygen carrier, alleviating tumor hypoxia and enhance PDT efficiency. More importantly, OFCCF nanocomposites based treatment has been proved to be a safe and effective strategy to inhibit tumor growth and open new directions for clinical cancer therapy.

Supplementary Information

The online version contains supplementary material available at <https://doi.org/10.1186/s12951-022-01392-y>.

Additional file 1: Table S1. Size of Nanoparticles. **Figure S1.** The SEM images of FeCOF. **Figure S2.** The SEM images of FeCOF@CaCO₃. **Figure S3.** (a) XPS spectra of FeCOF@CaCO₃. (b) XPS high-resolution scans of Ca 2p. **Figure S4.** The PXRD of FeCOF and FeCOF@CaCO₃. **Figure S5.** (a) N₂ adsorption and desorption isotherms at 77 K of FeCOF and FeCOF@CaCO₃. (b) Pore size distribution plots of FeCOF and FeCOF@CaCO₃. **Figure S6.** The Hydrodynamic diameters of FeCOF, FeCOF@CaCO₃ and FCCF. **Figure S7.** The zeta potential of FeCOF, FeCOF@CaCO₃ and FCCF. **Figure S8.** (a) The FCCF dispersed in water, PBS and cell culture medium (containing 10% serum) before and after 7 days incubation. (b) The TEM image of FCCF stored in cell culture medium (containing 10% serum) for a week. (c) The DLS was measured on day 0, 5 and 7 when FCCF was dispersed in water, PBS and cell culture medium (containing 10% serum). **Figure S9.** (a) SEM images of FCCF at pH 7.4, 6.5 and 5.5, related to Figure 2a. Data are presented as mean \pm SD (n = 3). **Figure S10.** (a) SEM images of FeCOF at pH 7.4, 6.5 and 5.5. Data are presented as mean \pm SD (n = 3). **Figure S11.** Oxygen release behaviour of OFCCF in solution. **Figure S12.** CLSM microimages of intracellular Ca²⁺ content in 4T1 cells. **Figure S13.** CLSM microimages of mitochondrial Ca²⁺ content in 4T1 cells. **Figure S15.** Quantitative analysis of the intracellular O₂ generation of 4T1 cells after various treatments based on the confocal images shown in Figure 3b by using imageJ, related to Figure 3b. **Figure S16.** Quantitative analysis of HIF-1 α protein expression, as the ratio of protein to β -actin from Western Blot results. Related to Figure 3c. P values were calculated by one-way analysis (*p<0.05, **p<0.01, ***p<0.001). **Figure S17.** Intracellular ROS production of 4T1 cells under normoxic and hypoxic conditions after various treatments. **Figure S18.** MPTP opening in mitochondria of 4T1 cells after different treatments. **Figure S19.** Mitochondrial membrane potential images of 4T1 cells after different treatments. **Figure S20.** Changes of intracellular ATP contents of 4T1 cells after being treated with PBS, L, COF+, FCCF, FCCF+ and OFCCF+ for 24 h. P values were calculated by one-way analysis (*p<0.05, **p<0.01, ***p<0.001). Data were represented as mean \pm SD (n = 4). **Figure S21.** Relative viabilities of L929 cells treated by incubation with COF and FCCF at different concentration for (a) 24 h and (b) 48 h. Data were represented as mean \pm SD (n = 6). **Figure S22.** The images of 4T1 cells after various treatments and stained with calcein-AM (live cells: green) and PI (dead cell: red). **Figure S23.** Quantitative analysis of Annexin V-FITC/PI co-stained 4T1 cells at 24 h after various treatments. **Figure S24.** Changes of body weight of mice in different groups after treatment. **Figure S25.** The tumor picture of mice before and after treatment in different groups (n = 8). **Figure S26.** (a) The photos of lung at the end of various treatments. (b) H&E-stained lung sections at the end of various treatments. Red arrows indicate the sites of tumor metastasis. **Figure S27.** Quantitative analysis of caspase 3, Bcl-2 and Cyt c protein expression, as the ratio of protein to β -actin from Western Blot results. Related to Figure 6 (f). **Figure S28.** ATP contents of tumor after being treated with PBS, L, COF+, FCCF, FCCF+ and OFCCF+. P values were calculated by one-way analysis (*p<0.05, **p<0.01, ***p<0.001). Data are presented as mean \pm SD (n = 4). **Figure S29.** (a) The HIF-1 α protein expression of tumor via western blotting analysis. (b) Quantitative analysis of HIF-1 α protein expression, as the ratio of protein to β -actin from Western Blot results. P values were calculated by one-way analysis (*p<0.05, **p<0.01, ***p<0.001). **Figure S30.** H&E stained images of the major organs, including heart, liver, spleen, lung, and kidney. Scale bar: 20 μ m. **Figure S31.** BALB/c mice were sacrificed after PBS and FCCF (NPs) treatment. Serum biochemistry data including Alanine aminotransferase (ALT), Aspartate aminotransferase (AST) and Alkaline phosphatase (ALP) as

hepatic function indicators and Blood urea nitrogen (BUN) as renal function indicators were measured. Blood hematological counts: Blood levels of White blood cells (WBC), Red blood cells (RBC), Hemoglobin (HGB), Hematocrit (HCT), Mean corpuscular volume (MCV), Mean corpuscular hemoglobin (MCH), Mean corpuscular hemoglobin concentration (MCHC) and Blood platelet (PLT). Data are presented as mean \pm SD ($n = 4$).

Acknowledgements

Not applicable.

Author contributions

These authors contribute equally. Correspondence: M.P, Y.Z and C.Z. Conceptualization, P.M, Y.Z and C.Z; writing—original draft preparation, Y.Z and S.J; experiments performing, all authors. All authors read and approved the final manuscript.

Funding

This project is financially supported by the National Natural Science Foundation of China (NSFC 21471145), Science and Technology Development Planning Project of Jilin Province (20170101179JC), and "Hundred Talents Program" of the Chinese Academy of Sciences.

Availability of data and materials

The data that support the findings of this study are available from the corresponding author upon reasonable request. Some data may not be made available because of privacy or ethical restrictions.

Declarations

Ethics approval and consent to participate

All animal experiment was performed strictly following the guidelines from the Animal Protection and Use Committee of Jilin University.

Consent for publication

All authors have approved the manuscript be submitted.

Competing interests

The authors declare that they have no competing interest in regard to this work.

Author details

¹Center of Infectious diseases and Pathogen Biology, Key Laboratory of Organ Regeneration and Transplantation of the Ministry of Education, The First Hospital of Jilin University, Changchun 130021, China. ²College of Animal Science, School of Pharmacy, Jilin University, Changchun 130022, China. ³State Key Laboratory of Rare Earth Resource Utilization, Changchun Institute of Applied Chemistry, Chinese Academy of Science, Changchun 130022, China. ⁴University of Science and Technology of China, Hefei 230026, People's Republic of China. ⁵Department of Gastroenterology and Hepatology, Zhongshan Hospital, Fudan University, Shanghai 200032, China. ⁶Clinical Medical College, Changchun University of Chinese Medicine, Changchun 130117, Jilin, China. ⁷Shanghai Institute of Liver Diseases, Shanghai 200001, China.

Received: 24 December 2021 Accepted: 21 March 2022

Published online: 12 April 2022

References

- Monteith GR. Prostate cancer cells alter the nature of their calcium influx to promote growth and acquire apoptotic resistance. *Cancer Cell*. 2014;26(1):1–2.
- Cui C, Merritt R, Fu L, Pan Z. Targeting calcium signaling in cancer therapy. *Acta Pharm Sin B*. 2017;7(1):3–17.
- Várnai GP, Golenár T, Roy S, Purkins G, Schneider TGT, Balla G. Hajnóczky, imaging interorganelle contacts and local calcium dynamics at the ER-mitochondrial interface. *Mol. Cell*. 2010;39(1):121–32.
- Parkash J, Asotra K. Calcium wave signaling in cancer cells. *Life Sci*. 2010;87(19–22):587–95.
- Lyu Y, Xie C, Chechetka SA, Miyako E, Pu K. Semi-conducting polymer nanobioconjugates for targeted photothermal activation of neurons. *J Am Chem Soc*. 2016;138(29):9049–52.
- Ma Z, Han K, Dai X, Han H. Precisely striking tumors without adjacent normal tissue damage via mitochondria templated accumulation. *ACS Nano*. 2018;12(6):6252–62.
- Ma Z, Zhang J, Zhang W, Foda MF, Zhang Y, Ge L, Han H. Intracellular Ca^{2+} cascade guided by NIR-II photo-thermal switch for specific tumor therapy. *iScience*. 2020;23(5):101049.
- Gogvadze V, Orrenius S, Zhivotovsky B. Mitochondria as targets for chemotherapy. *Apoptosis*. 2009;14(4):624–40.
- Agarwal A, Wu PH, Hughes EG, Fukaya M, Tischfield MA, Langseth AJ, Wirtz D, Bergles E. Transient opening of the mitochondrial permeability transition pore induces microdomain calcium transients in astrocyte processes. *Neuron*. 2017;93(3):587–605.
- Halestrap AP, Clarke SJ, Javadov SA. Mitochondrial permeability transition pore opening during myocardial reperfusion—a target for cardioprotection. *Cardiovascular Res*. 2004;61(3):372–85.
- Pérez MJ, Quintanilla RA. Development or disease: duality of the mitochondrial permeability transition pore. *Biol. Dev*. 2017;426(1):1–7.
- Hurst S, Hoek J, Sheu SS. Mitochondrial Ca^{2+} and regulation of the permeability transition pore. *J Bioenerg Biomembr*. 2017;49(1):27–47.
- Xu H, Cui S, Zhang Y, Ren J. Mitochondrial Ca^{2+} regulation in the etiology of heart failure: physiological and patho-physiological implications. *Acta Pharmacol Sin*. 2020;41(10):1301–9.
- Bernardi P, Rasola A, Forte M. The mitochondrial permeability transition pore: channel formation by F-ATP synthase, integration in signal transduction, and role in pathophysiology. *G Physiol Rev*. 2015;95(4):1111–55.
- Shanmughapriya S, Rajan S, Hoffman NE, Higgins AM, Tomar D, Nemani N, Hines KJ, Smith D, Eguchi JA, Vallem S. SPG7 is an essential and conserved component of the mitochondrial permeability transition pore. *Mol Cell*. 2015;60(1):47–62.
- Biasutto L, Azzolini M, Szabo I, Zoratti M. The mitochondrial permeability transition pore in AD 2016: an up-date. *Acta Pharm Sin B*. 2016;1863(10):2515–30.
- Li Y, Sun J, Wu R, Bai J, Hou Y, Zeng Y, Zhang Y, Wang X, Wang Z, Meng X. Mitochondrial MPPT: a novel target of ethnomedicine for stroke treatment by apoptosis inhibition. *Front Pharmacology*. 2020;11:352.
- Zhao Y, Luo Z, Li M, Qu Q, Ma X, Yu SH, Zhao Y. A preloaded amorphous calcium carbonate-doxorubicin@silica nanoreactor for pH-responsive delivery of an anticancer drug. *Angew Chem Int Ed*. 2015;54(3):919–22.
- Dong Z, Feng L, Hao Y, Li Q, Chen M, Yang Z, Zhao H, Liu Z. Synthesis of $CaCO_3$ -based nanomedicine for enhanced sonodynamic therapy via amplification of tumor oxidative stress. *Chem*. 2020;6(6):1495–7.
- Chang M, Hou Z, Jin D, Zhou J, Wang M, Shu M, Ding B, Li C, Lin J. Colorectal tumor microenvironment-activated bio-decomposable and mMetabolizable $Cu_2O@CaCO_3$ nanocomposites for synergistic oncotherapy. *Adv Mater*. 2020;32(43):2004647.
- Dong Z, Feng L, Hao Y, Chen M, Gao M, Chao Y, Zhao H, Zhu W, Liu J, Liang C, Zhang Q, Liu Z. Synthesis of hollow biomimetic $CaCO_3$ -polydopamine nanoparticles for multimodal imaging-guided cancer photodynamic therapy with reduced skin photosensitivity. *J Am Chem Soc*. 2018;140(6):2165–78.
- Wan X, Zhong H, Pan W, Li Y, Chen Y, Li N, Tang B. Programmed release of dihydroartemisinin for synergistic cancer therapy using a $CaCO_3$ mineralized metal-organic framework. *Angew Chem Int Ed*. 2019;131(40):14272–7.
- Lybaert L, Ryu KA, Nuhn L, Rycke RD, Wever OD, Chon AC, Esser-Kahn AP, Geest BG. Cancer cell lysate entrapment in $CaCO_3$ engineered with polymeric TLR-agonists: immune-modulating microparticles in view of personalized antitumor vaccination. *Chem Mater*. 2017;29(10):4209–17.
- Zorov DB, Juhaszova MS, Sollott J. Mitochondrial ROS-induced ROS release: an update and review. *Bba-Bioenergetics*. 2006;1757(5–6):509–17.
- Zeng Z, Zhang C, Li J, Cui D, Jiang Y, Pu K. Activatable polymer nanoenzymes for photodynamic immunometabolic cancer therapy. *Adv Mater*. 2021;33(4):2007247.
- Li Y, Sun P, Zhao L, Yan X, Ng DKPP, Lo C. Ferric ion driven assembly of catalase-like supramolecular photosensitizing nanozymes for combating hypoxic tumors. *Angew Chem Int Ed*. 2020;132(51):23228–38.

27. Brown SB, Brown EA, Walker I. The present and future role of photodynamic therapy in cancer treatment. *Lancet Oncol.* 2004;5(8):497–508.
28. Singhal S, Nie S, Wang M. Nanotechnology applications in surgical oncology. *Annu Rev Med.* 2010;61:359–73.
29. Wu W, Yu L, Jiang Q, Huo M, Lin H, Wang L, Chen Y, Shi J. Enhanced tumor-specific disulfiram chemotherapy by in situ Cu²⁺ chelation-initiated nontoxicity-to-toxicity transition. *J Am Chem Soc.* 2019;141(29):11531–9.
30. Wang Z, Zhang Y, Ju E, Liu Z, Cao F, Chen Z, Ren J, Qu X. Biomimetic nano-flowers by self-assembly of nanozymes to induce intracellular oxidative damage against hypoxic tumors. *Nat Commun.* 2018;9(1):3334.
31. Yang S, Tang Z, Hu C, Zhang D, Shen N, Yu H, Chen X. Selectively potentiating hypoxia levels by com-bretastatin A4 nanomedicine: toward highly enhanced hypoxia-activated prodrug tirapazamine therapy for metastatic tumors. *Adv Mater.* 2019;31(11):1805955.
32. Sun J, Du K, Diao J, Cai X, Feng F, Wang S. GSH and H₂O₂ co-activatable mitochondria-targeted photodynamic therapy under normoxia and hypoxia. *Angew Chem Int Ed.* 2020;59(22):12122–8.
33. Liu W, Liu T, Zou M, Yu W, Li C, He Z, Zhang M, Liu M, Li Z, Feng J, Zhang X. Aggressive man-made red blood cells for hypoxia-resistant therapy. *Adv Mater.* 2018;30(35):802006.
34. Song X, Feng L, Liang C, Yang K, Liu Z. Ultrasound triggered tumor oxygenation with oxygen-shuttle nanoporous-fluorocarbon to overcome hypoxia-associated resistance in cancer therapies. *Nano Lett.* 2016;16(10):6145–53.
35. Cai X, Xie Z, Ding B, Shao S, Liang S, Pang M, Lin J. Monodispersed copper(I)-based nano metal-organic framework as a biodegradable drug carrier with enhanced photodynamic therapy efficacy. *Adv Sci.* 2019;6(15):1900848.
36. Guan Q, Zhou L, Li W, Li Y, Dong Y. Covalent organic frameworks (COFs) for cancer therapeutics. *Chem Eur J.* 2020;26(25):5583–91.
37. Liu S, Hu C, Liu Y, Zhao X, Pang M. One-pot synthesis of DOX@covalent organic framework with enhanced chemotherapeutic efficacy. *J Chem Eur J.* 2019;25(17):4315–9.
38. Hu C, Zhang Z, Liu S, Liu X, Pang M. Monodispersed CuSe sensitized covalent organic framework photosensitizer with an enhanced photodynamic and photothermal effect for cancer therapy. *ACS Appl Mater Interfaces.* 2019;11(26):23072–82.
39. Hu C, Cai L, Liu S, Pang M. Integration of a highly mono-disperse covalent organic framework photosensitizer with cation exchange synthesized Ag₂Se nanoparticles for enhanced phototherapy. *Chem Commun.* 2019;55(62):9164–7.
40. Liu S, Zhou Y, Hu C, Cai L, Pang M. Covalent organic framework-based nanocomposite for synergistic photo-, chemodynamic-, and immunotherapies. *ACS Appl Mater Interfaces.* 2020;12(39):43456–65.
41. Wang P, Zhou F, Guan K, Wang Y, Fu X, Yang Y, Yin X, Song G, Zhang X, Tan W. In vivo therapeutic response monitoring by a self-reporting upconverting covalent organic framework nanoplatfrom. *Chem Sci.* 2020;11(5):1299–306.
42. Bai L, Phua SZFW, Lim Q, Jana A, Luo Z, Tham HP, Zhao L, Gao Q, Zhao Y. Nanoscale covalent organic frameworks as smart carriers for drug delivery. *Chem Commun.* 2016;52(22):4128–31.
43. Dong Z, Feng L, Zhu W, Sun X, Gao M, Zhao H, Chao Y, Liu Z. CaCO₃ nanoparticles as an ultra-sensitive tumor-pH-responsive nanoplatfrom enabling real-time drug release monitoring and cancer combination therapy. *Biomaterials.* 2016;110:60–70.
44. Guan Q, Zhou L, Lv F, Li W, Li Y, Dong Y. A glycosylated covalent organic framework equipped with BODIPY and CaCO₃ for synergistic tumor therapy. *Angew Chem Int Ed.* 2020;59(41):18042–7.
45. Wang S, Ni D, Yue H, Luo N, Xi X, Wang Y, Shi M, Wei W, Ma G. Exploration of antigen induced CaCO₃ nanoparticles for therapeutic vaccine. *Small.* 2018;14(14):1704272.
46. Peng J, Fumoto S, Suga T, Miyamoto H, Kuroda N, Kawakami S, Nishida K. Targeted co-delivery of protein and drug to a tumor in vivo by sophisticated RGD-modified lipid-calcium carbonate nanoparticles. *J Control Release.* 2019;302:42–53.
47. Jiang Y, Huo S, Hardie J, Liang XJ, Rotello VM. Progress and perspective of inorganic nanoparticle-based siRNA delivery systems. *Expert Opin Drug Del.* 2016;13(4):547–59.
48. Shaik MF, Yanamala VR, Rajanikant GK. CypD: the key to the death DOOR CnS neurological disorders-drug targets. *Cns Neurol Disord-dr.* 2015;14(5):654–63.

Publisher's Note

Springer Nature remains neutral with regard to jurisdictional claims in published maps and institutional affiliations.

Ready to submit your research? Choose BMC and benefit from:

- fast, convenient online submission
- thorough peer review by experienced researchers in your field
- rapid publication on acceptance
- support for research data, including large and complex data types
- gold Open Access which fosters wider collaboration and increased citations
- maximum visibility for your research: over 100M website views per year

At BMC, research is always in progress.

Learn more biomedcentral.com/submissions

